Coda-Q in the 2.5s -20s period band from seismic noise - Application to the greater Alpine area

Dorian Soergel, Helle A Pedersen, Laurent Stehly, Ludovic Margerin, Anne Paul, Alparray Working Group

Geophysical Journal International

Geophys. J. Int. (2020) **220,** 202–217
Advance Access publication 2019 October 04
GJI Seismology

doi: 10.1093/gji/ggz443

Coda-Q in the 2.5–20 s period band from seismic noise: application to the greater Alpine area

D. Soergel,[1] H. A. Pedersen,[1] L. Stehly,[1] L. Margerin,[2] A. Paul[1] and AlpArray Working Group[*]

[1] *Univ. Grenoble Alpes, Univ. Savoie Mont Blanc, CNRS, IRD, IFSTTAR, ISTerre,* 38000 *Grenoble, France. E-mail: dorian.soergel@univ-grenoble-alpes.fr*
[2] *Institut de Recherche en Astrophysique et Planétologie, Université Paul Sabatier, CNRS, CNES, Toulouse, France*

Accepted 2019 October 1. Received 2019 August 5; in original form 2019 April 20

SUMMARY

Coda-Q is used to estimate the attenuation and scattering properties of the Earth. So far focus has been on earthquake data at frequencies above 1 Hz, as the high noise level in the first and second microseismic peak, and possibly lower scattering coefficient, hinder stable measurements at lower frequencies. In this work, we measure and map coda-Q in the period bands 2.5–5 s, 5–10 s and 10–20 s in the greater Alpine region using noise cross-correlations between station pairs, based on data from permanent seismic stations and from the temporary AlpArray experiment. The observed coda-Q for short interstation distances is independent of azimuth so there is no indication of influence of the directivity of the incoming noise field on our measurements. In the 2.5–5 s and 5–10 s period bands, our measurements are self-consistent, and we observe stable geographic patterns of low and high coda-Q in the period bands 2.5–5 s and 5–10 s. In the period band 10–20 s, the dispersion of our measurements increases and geographic patterns become speculative. The coda-Q maps show that major features are observed with high resolution, with a very good geographical resolution of for example low coda-Q in the Po Plain. There is a sharp contrast between the Po Plain and the Alps and Apennines where coda-Q is high, with the exception a small area in the Swiss Alps which may be contaminated by the low coda-Q of the Po Plain. The coda of the correlations is too short to make independent measurements at different times within the coda, so we cannot distinguish between intrinsic and scattering Q. Measurements on more severely selected data sets and longer time-series result in identical geographical patterns but lower numerical values. Therefore, high coda-Q values may be overestimated, but the geographic distribution between high and low coda-Q areas is respected. Our results demonstrate that noise correlations are a promising tool for extending coda-Q measurements to frequencies lower than those analysed with earthquake data.

Key words: Europe; Coda waves; seismic attenuation; seismic noise; surface waves and free oscillations; wave scattering and diffraction.

1 INTRODUCTION

Since its inception by Aki & Chouet (1975), the coda quality factor *Qc* has arguably become one if not the most used measure of seismic attenuation around the world (see Herraiz & Espinosa 1987; Fehler *et al.* 1992; Mikesell *et al.* 2012, for reviews). In their seminal publication, Aki & Chouet (1975) demonstrate conclusively that, at sufficiently long lapse-time t after the energy release at the source, the energy envelope $E(f, t)$ of late seismic arrivals (known as coda waves) observed in a narrow frequency band $f \pm \Delta f$ follows an algebro-exponential decay of the form:

$$E\ (f,t) = S(f)\,\mathrm{e}^{-\frac{2\pi t f}{Q(f)}} t^{-\alpha}, \qquad (1)$$

where the exponent α typically varies between 1 and 2 depending on the type of waves (surface waves or body waves) and scattering model (single-scattering or diffusion). The coda wavefield itself can be shown to obey Gaussian statistics with very good accuracy (Anache-Menier *et al.* 2009; Obermann *et al.* 2014). This statistical property follows logically from the physical interpretation of the coda as a superposition of a large number of scattered waves with random phase, by application of the central limit theorem. Using the Gaussian hypothesis, it is straightforward to demonstrate that the

[*] https://www.alparray.ethz.ch

energy envelope obeys an exponential distribution, which explains quantitatively the large fluctuations of the coda intensity observed in the data. A practical implication of these fluctuations is that the parameter α cannot be determined unambiguously from the data alone, but has to be fixed in advance based on a physical model. Aki & Chouet (1975) proposed several simple scattering scenarios underpinning formula (1). In the single scattering model, α equals 1 or 2 depending on the type of waves that dominate the coda: surface waves for the former, body waves for the latter. Single scattering also implies the relation:

$$\frac{1}{Q_c} = \frac{1}{Q_i} + \frac{1}{Q_{sc}}$$

suggesting that Q_c is a measure of total attenuation. In sharp contrast with single scattering, formula (1) may also be explained by a diffusion model where a large number of scattering events occur between source and detection. In the diffusion regime, α depends on the dimensionality of the medium. In half-space geometry, $\alpha = 3/2$ whereas in waveguide geometry $\alpha = 1$. Furthermore the diffusion model implies:

$$\frac{1}{Q_c} = \frac{1}{Q_i}$$

suggesting that in this regime Q_c is a measure of absorption in the medium.

After Aki and Chouet's discovery, it has long been considered that single scattering was the most appropriate model for the coda on Earth. This situation changed radically in the mid-nineties with the introduction of quantitative methods of measurement of scattering and absorption properties in the framework of radiative transfer theory (Wu & Aki 1988; Fehler *et al.* 1992). It became clear that multiple scattering plays a fundamental role in the generation of coda waves and also that the interpretation of Q_c is not univocal. On the one hand extensive data analyses in Japan by Carcole & Sato (2010) show very good coincidence between Q_c and Q_i in agreement with the predictions of the diffusion model. On the other hand, Calvet & Margerin (2013) show on a data set from the Pyrenees that Q_c agrees well with Q_i only when scattering is not too strongly anisotropic and the coda window is chosen at sufficiently long lapse time. Independently of its physical interpretation, Q_c remains an interesting proxy for the mapping of spatial variations of attenuation.

In earthquake seismology, Q_c is generally observed in the 1–20 Hz frequency band, but imaging attenuation at longer periods is of crucial importance for seismic hazard calculations, as the resonance frequencies of tall buildings can lie below 1 Hz. It also gives important insights on the attenuating and scattering properties of rocks. The detection of the coda at longer period is hampered by the fact that the scattering coefficient decreases rapidly with T (as shown by theoretical studies in random media, e.g. Stanke & Kino 1984) and by the strong permanent excitation of ambient noise by swell and oceanic wave interactions between 5 and 15 s period. In fact, this period band represents an observational gap for the seismic Q, which makes it difficult to pinpoint the dominant physical mechanisms at the origin of seismic attenuation. Seismic interferometry (Campillo & Paul 2003; Shapiro & Campillo 2004) offers an attractive alternative to study the attenuation of seismic waves, particularly in the period band of ocean-generated microseismic noise. While most efforts so far have focused on the determination of attenuation based on the propagation properties of ballistic waves (e.g. Prieto & Beroza 2008; Cupillard & Capdeville 2010; Denolle *et al.* 2013; Liu *et al.* 2015; Stehly & Boue 2017), it is clear that cross and autocorrelations of the ambient noise wavefields also possess a coda that could fruitfully complement the standard analyses. This coda has in fact been exploited for more than a decade in monitoring techniques such as passive image interferometry (Sens-Schönfelder & Wegler 2006). Despite the success of seismic interferometry and passive image interferometry, not much attention has been paid to the decay properties of the coda of ambient noise correlograms. It is the purpose of this paper to bridge this gap and to demonstrate that spatially coherent variations of coda attenuation may be extracted from ambient noise data thanks to appropriate data selection and processing procedures.

2 DATA AND DATA PROCESSING

2.1 Data

We use continuous data (vertical component) recorded over twelve months, between July 2016 and June 2017. During this period, a large part of the AlpArray temporary seismic experiment was installed and running, hence the high station density in the Alpine region. A total of 736 stations, located in the area (2°E–20°E, 35°N–55°N), are used, with 542 permanent and 194 temporary AlpArray stations. The AlpArray seismic network is the combination of ∼350 permanent broad-band stations and ∼280 temporary broad-band stations that span over the greater alpine area from Massif Central in the west to Pannonian Basin in the east, and Corsica in the south to north of the Czech Republic (Hetenyi *et al*. 2018). The temporary array was designed to obtain a homogeneous coverage with station spacing 52 km. Because of its homogeneous distribution, regular spacing and long residence time (2–3 yr) the AlpArray seismic network is well suited for seismic noise interferometry. Note that a larger number of stations is processed, but the 736 stations are those for which we can extract signal from correlations. We additionally use 4 yr of data from a subset of permanent seismic stations to study convergence of observed coda-Q (see Section 4.2). The data are distributed by EIDA (European Integrated Data Archive), a service of ORFEUS (www.orfeus-eu.org). Fig. 1 shows the station distribution.

2.2 Pre-processing and noise correlations

Before computing the correlations, we pre-process the noise recorded by each station in two main steps. First, each daily record is detrended, low-pass filtered (0.45 Hz corner frequency), decimated to 1 Hz and corrected for instrument response. This reduced data set is stored to disk.

One specific difficulty of noise correlations is that they require handling of transient high amplitude signals such as earthquakes or storms. After tests, we choose a pre-processing that we will refer to as '*comb filter pre-processing*': the signal is filtered into several period bands (3–5, 5–10, 10–20, 20–40, 40–80 and 80–200 s), each of the filtered signals is normalized by its envelope, and the six filtered and normalized signals are finally stacked. This pre-processing was chosen specifically since it achieves broad-band signals that do not have dominating transients, therefore well adapted to obtain broad-band correlations for Green's function estimation.

It has been demonstrated that convergence of the correlations is faster in shorter time windows as compared to daily time windows (e.g. Poli *et al.* 2012). The window length must remain large as compared to the maximum lag time used, in our case we use lag

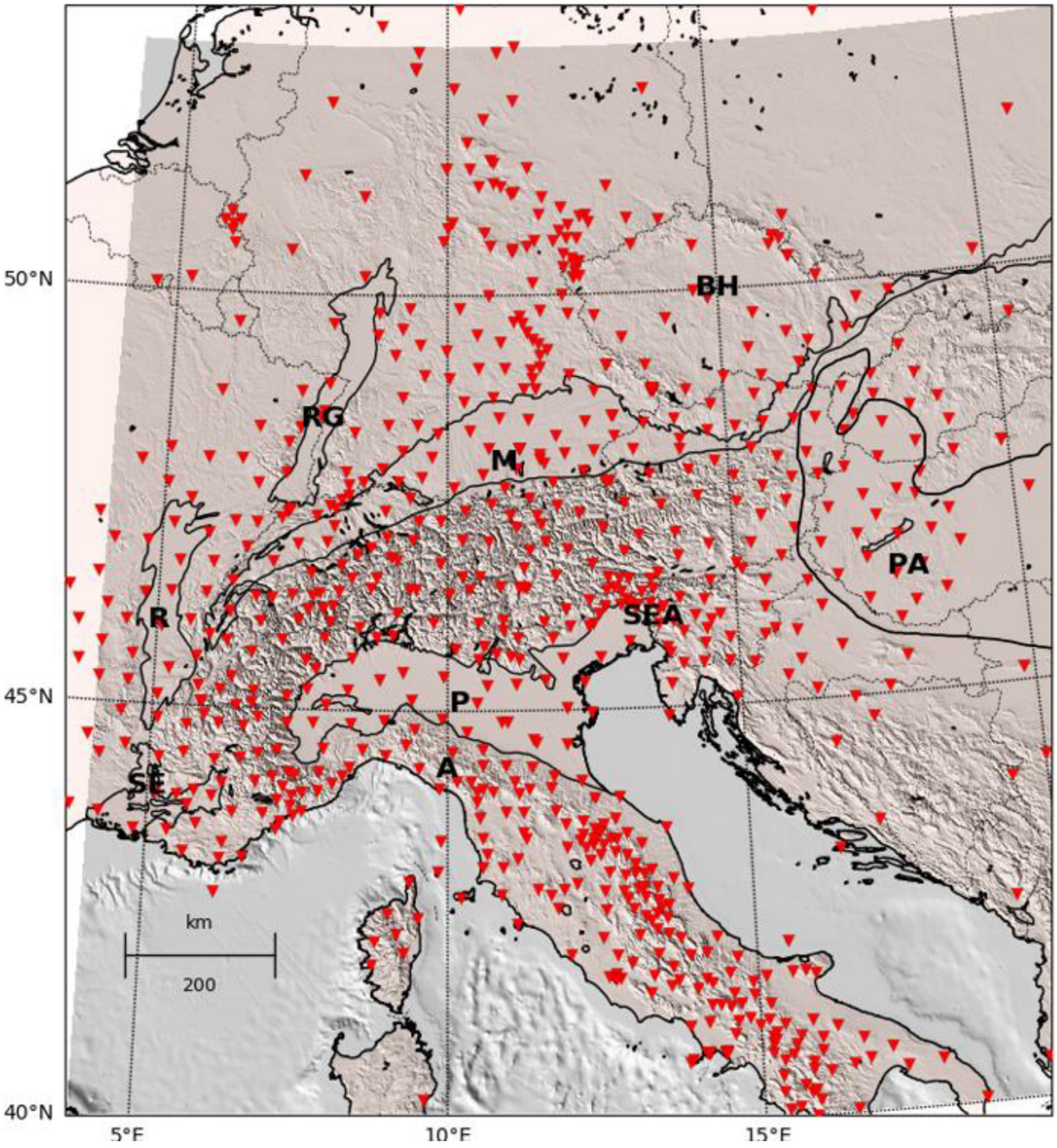

Figure 1. Map of stations used in this study. The network is composed of permanent stations as well as temporary stations of AlpArray (AlpArray Seismic Network 2015; Hetényi *et al.* 2018). The references to the data sets can be found in Section 6. Geographic locations mentioned in the text are: the Po Plain (P) and the southeastern Alps (SEA), the Bohemian Massif (BH), the southeast France Basin (SE), the Rhone Valley (R), the Rhine Graben (RG), the Molasse Basin (M), the Pannonian Basin (PA) and the Appenines (A). The outlines of the Bohemian Massif to the west and north correspond roughly to the frontiers of the Czech Republic (national boundaries shown as thin dotted lines).

times of up to ±3000 s. We therefore calculate cross-correlations between each pair of stations using 4 hr windows, normalize and stack them, to obtain one correlation trace for each station pair. We thus obtain ∼500 000 correlations, where for each one we keep track of the total number of days stacked.

Fig. 2 shows the seismic section of correlations in the three frequency bands we use in this study. It is known that the Rayleigh wave component of the seismic noise in northern Europe is dominated by waves emitted by sources in the North Atlantic Ocean during the winter season, and more widely distributed if the whole year is considered (e.g. Friedrich *et al.* 1998; Stehly *et al.* 2006; Pedersen *et al.* 2007; Kedar *et al.* 2008; Landès *et al.* 2010; Hillers *et al.* 2012; Retailleau *et al.* 2017). The correlations are therefore oriented so that the causal signal (positive times) corresponds to seismic waves propagating away from 300° azimuth, that is from the half space which contains the main noise source area. As expected, the Rayleigh wave emerges very clearly in the causal part and less so in the anticausal part, especially at longer interstation distances.

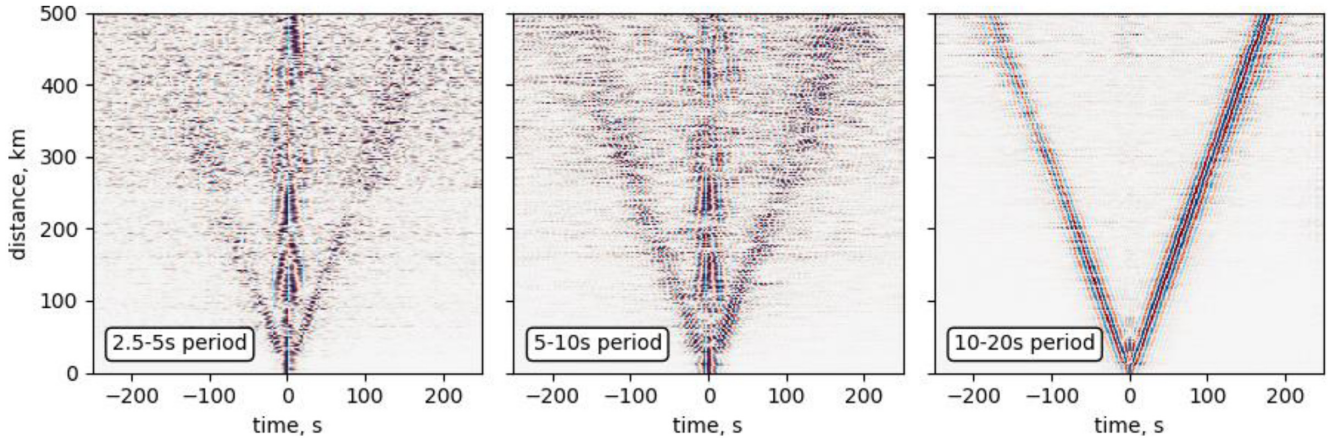

Figure 2. Seismic section of correlations in the 2.5–5 s (left-hand panel), 5 s–10 s (centre panel) and 10–20 s (right-hand panel) period bands. The traces are stacked in bins of 1 km and normalized by their maximum. All correlations have been oriented so that the causal part points away from 300° of azimuth; that is the direction which approximately corresponds to the dominant direction of the noise sources. We clearly see the dispersive Rayleigh waves. As expected, the amplitude of the causal part is higher than the anticausal part, especially for longer distances. The plot of seismic sections for the selected data set (see Section 2.3) is shown as Fig. S1.

2.3 Coda-Q measurements

The coda-Q measurement is carried out independently in three period bands within the first (10–20 s) and second (2.5–5 s, 5–10 s) microseismic peaks. The processing and our observations are exemplified for the 5–10 s frequency band, where the measurement of coda-Q is of highest quality. We analyse the correlations independently for the positive and negative times, so in the following, the term 'trace' refers to either the positive or the time-reversed negative correlation. Unless otherwise stated, we present examples and results on traces that are bandpass filtered between 5 and 10 s period. We have a total of ∼1 000 000 such traces. Fig. 3 shows the different steps of the coda-Q measurement for a single trace.

For each trace, the arrival time of the direct Rayleigh wave is estimated, within a window corresponding to a propagation velocity of 1.5–5 km s^{-1}, as the time where the envelope of the trace is maximum (green dashed line in Fig. 3b). The energy as a function of time (grey line in Fig. 3b) is calculated as the square of the trace, normalized by the average energy in the last quarter (2250–3000 s) which is stable over this interval. After normalization, the average energy in the last quarter of the signal is 1 (dashed red line in Fig. 3b). The normalized energy is then smoothed (blue line in Fig. 3b) with a time window which has a length of 16 times the dominant period (after filtering, as stated above). In the following the signal-to-noise ratio (SNR) is defined as the value of the smoothed energy at the arrival time of the direct Rayleigh wave, after normalization.

Fig. 4 shows plots of trace density of correlations in the Gräfenberg area (11°E–12°E, 49°N–50°N) for different frequency bands, using only correlations with station distances between 50 and 200 km which passed all selection criteria detailed later in this paragraph. We observe three different regimes of the smoothed energy, as already pointed out in Sens-Schönfelder & Wegler (2006): the main arrival (the ∼200 s duration of this peak is created by the smoothing), followed by a gentle slope, corresponding to the coda, over a few hundred seconds, and finally followed by a smooth transition into the background noise.

To estimate coda-Q, we define the beginning of the coda window as 120 s (vertical green line in Fig. 3b) after the main arrival. This choice, checked by visual inspection on a large number of traces and trace density plots such as those shown in Fig. 4, is motivated by the need of avoiding strong influence of the main peak. It also corresponds to 16 times the central period of the 5–10 s period band (which is the smoothing length). The window length is 400 s (600 s for 10–20 s period band), chosen as the longest possible window length while staying above the noise level. These window lengths correspond to a lower limit of 40 periods in the 5–10 s band and of 30 periods in the 10–20 s band. In comparison, Mayor *et al.* (2016), who used earthquake data, used an observation window of 50 s in a frequency band between 1 and 32 Hz that corresponds to 50 and 1600 periods.

Within the defined coda window, we measure coda-Q following the classical procedure of Aki & Chouet (1975). It models the coda energy decay with the equation $E\ (f,t) = S(f)e^{-\frac{2\pi f}{Q(f)}t}t^{-\alpha}$ (eq. 1) where E here is the normalized energy, $S(f)$ is a constant which depends on source magnitude, site effects and frequency, t is the time since the event, f is the frequency of the signal, Q is coda-Q and α is an algebraic coefficient (Aki & Chouet 1975) that depends on the type of waves (surface waves or body waves) and scattering model (single-scattering or diffusion). Since we are using noise cross-correlations instead of earthquake measurements, the time since the event is replaced by the correlation time. Coda-Q for the trace is obtained by least-squares fit of the logarithm of $E(f,t)\ t^{\alpha}$. We use $\alpha = 1$ (corresponding to single-scattering of surface waves) since we expect surface waves to be dominant and since our coda window is close to the Rayleigh-wave arrival.

At this stage, we exclude from further analysis a subset of correlations, using three criteria. First, as we will only use short interstation distances in the mapping we exclude traces that correspond to distances of more than 3000 km. Secondly, we exclude traces for which the coda energy (smoothed over a 40-period-long window) falls below the noise level within the analysis window. Third, we also reject all coda-Q measurements with coda-Q values smaller than 10 or bigger than 2000 (4000 in the 2.5–5 s period band). This selection reduces the original data set of ∼1 000 000 traces by ∼87 per cent (2.5–5 s), 56 per cent (5–10 s) and 51 per cent (10–20 s). These rejection rates can be compared with those of Mayor *et al.* (2016) who chose a subset of 50 per cent of their earthquake coda data set for the mapping of coda-Q, decreasing the number of coda measurements from ∼40 000 to ∼20 000. The seismic sections after this selection are shown in Fig. S1.

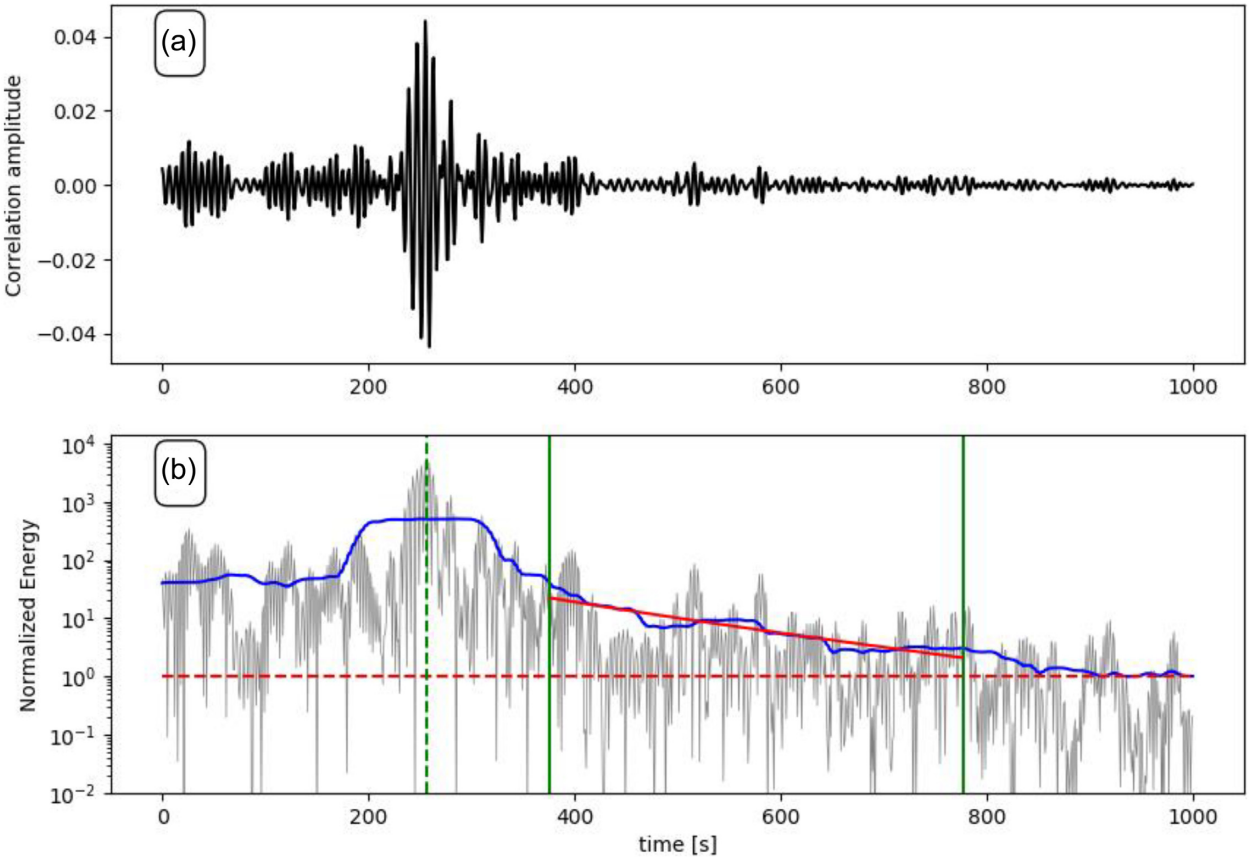

Figure 3. Example of processed trace (station couple CH.BERGE—Z3.A263A, interstation distance 703 km). (a) Correlation filtered between 5 and 10 s. (b) Same trace squared (grey) and smoothed (blue). The red line corresponds to the modeled coda decay after inversion for coda-Q. The green lines mark the borders of the interval in which the coda is fitted. Green dashed line: main arrival. Red dashed line: noise level (normalized to 1). Note the logarithmic vertical scale in the bottom plot.

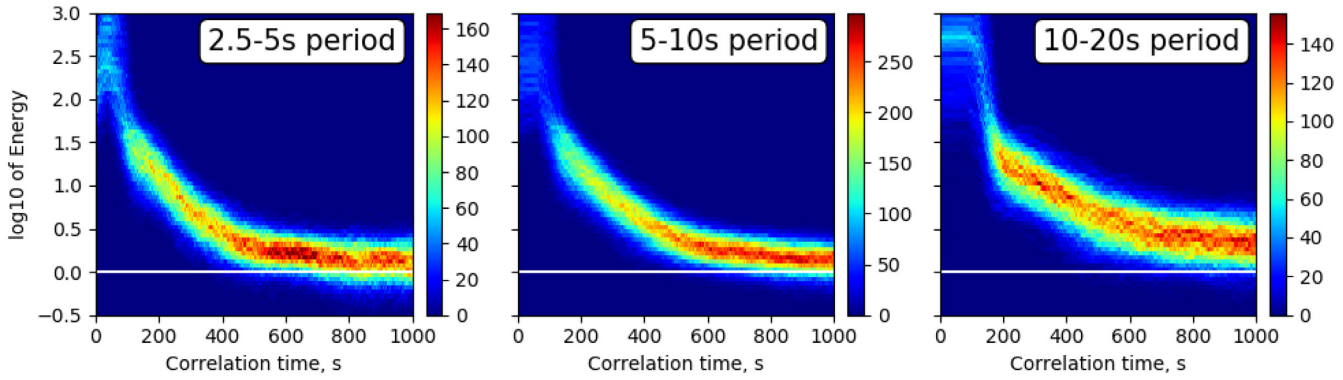

Figure 4. Smoothed energy (log scale) as a function of time (correlation time) for correlations for which one of the stations is located in the Gräfenberg area (11°E–12°E, 49°N–50°N) and the interstation distance is between 50 and 200 km. This plot uses only traces for which the trace is above the noise level in the coda window and where the measured coda-Q is in the acceptable coda-Q range. The traces are shown in the form of trace density where the colour of each pixel indicates the number of traces crossing it. The white line corresponds to the noise level.

As the fit to the energy depends both on the term $t^{-\alpha}$ and on coda-Q, it is at this stage relevant to discuss the choice of $\alpha = 1$. Fig. 5 shows the equivalent to Fig. 4 (5–10 s periods) within the 400 s long coda window, but this time corrected for the term t^{-1}. The remaining decay shows a clear linear decrease with time, which validates our choice for α. However, the spread of the data means that α cannot be constrained very strictly. Choice of for example $\alpha = 1.5$ (diffusion regime) implies an overall increase of the estimated coda-Q for all traces and an increase of the curvature upwards on Fig. 5, which does not seem appropriate.

Fig. 6(left-hand panel) shows the distribution of coda-Q (5–10 s period) after data selection. In contrast with earthquake studies, we need to verify that coda-Q is independent of azimuth, due to the systematic directional dependence of incoming energy. Considering the 50–200 km distance range (in blue), coda-Q is indeed independent of azimuth as shown in Fig. 6(centre panel). This demonstrates

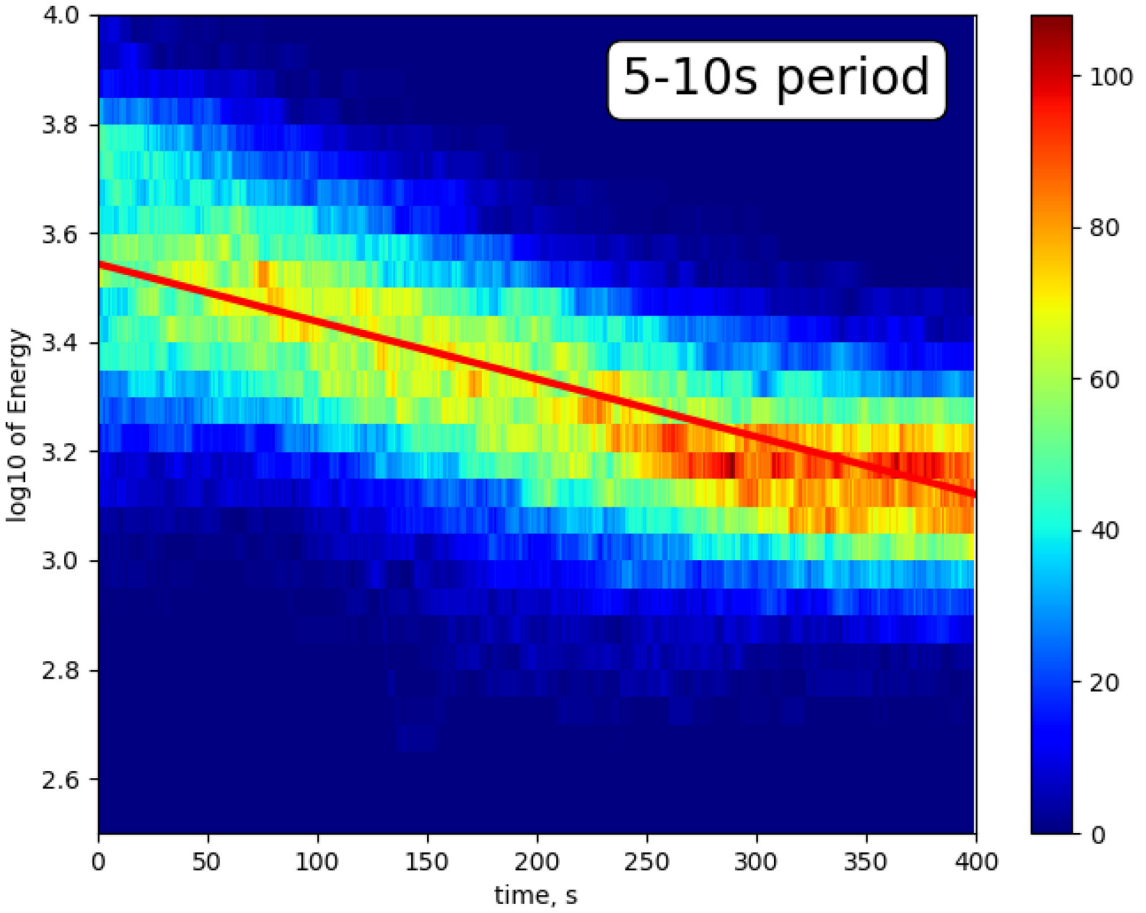

Figure 5. Smoothed energy (log scale) as a function of time (lag time after main arrival), after correction for the $t^{-\alpha}$ term, for the same traces as in Fig. 4, and for the 5–10 s period band. The traces are shown in the form of trace density where the colour of each pixel indicates the number of traces crossing it. The red line corresponds to the (geometrical) average of coda-Q observed on the same traces.

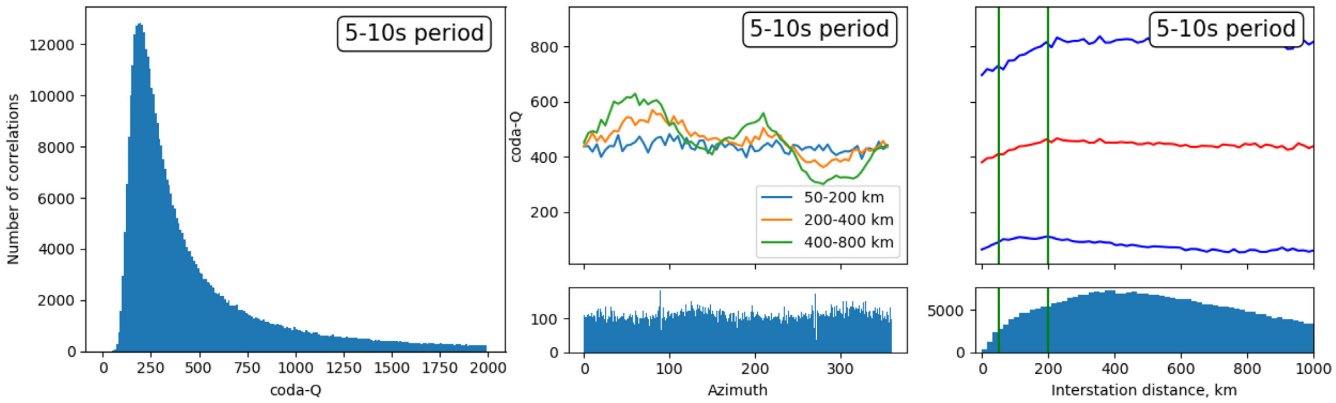

Figure 6. Left-hand panel: histogram of coda-Q. Centre panel: coda-Q as a function of azimuth in the distance bands 50–200 km, 200–400 km and 400–800 km, and histogram of azimuth (in the distance range 50–200 km). For longer distances, azimuths corresponding to the main noise sources have lower coda-Q values, whereas azimuths opposed have higher ones. This is most likely due to the difference in signal-to-noise ratio, as if the coda window is dominated at least partly by noise the measured coda-Q will be higher. As compared to Fig. 2, the anticausal part corresponds to the data for azimuth between 30° and 210° whereas the causal part corresponds to data for azimuths between 210° and 360° and between 0° and 30°. Right-hand panel: coda-Q as a function of distance, and histogram of distances (green lines show the 50–200 km range). The red line corresponds to the average coda-Q and the blue lines corresponds to the average ±1 standard deviation.

that secondary observables such as coda-Q can be independent of azimuth even though the main arrival is not. At longer distances, there is a visible dependence of coda-Q with azimuth. This dependence corresponds to the distribution of noise sources: at longer distances, there is a bias towards lower coda-Q for azimuths corresponding to the main noise sources, and a bias towards higher coda-Q in the opposite direction. For short distances, the azimuthal coverage is very homogeneous over the whole area, whereas for

longer distances the station distribution leads to uneven azimuthal coverage. For example, there are no long SW–NE oriented profiles that sample large parts of the Italian peninsula while many NW–SE profiles sample that same area. In addition, the azimuth distribution is poor for stations close to the edge of the array, and this effect increases if we use longer interstation distances. Therefore, the azimuth dependence at distances longer than 200 km may reflect that different azimuths do not sample exactly the same regions. The independence of coda-Q with azimuth in the 50–200 km distance range demonstrates that, at least in our case, the distribution of noise sources does not influence the value of coda-Q. Based on these observations, we restrict ourselves to interstation distances of 50–200 km for analysing geographical variations in coda-Q; this selection corresponds to 18 433 coda-Q measurements in the 2.5–5 s period band, 40 699 in the 5–10 s period band and 31 524 in the 10–20 s period band. The observed independence of coda-Q with azimuth is in agreement with Colombi *et al.* (2014) who used both numerical simulations and field data to show that the coda of correlations is very stable in terms of waveforms with respect to source distribution. Fig. 6(right-hand panel) shows that for short interstation distances, used for mapping (50–200 km, shown with green lines), coda-Q (average in red, standard deviation in blue) is slightly increasing with distance. Consequently, we will have a (small) systematic bias in regions with long interstation distances towards higher coda-Q values. However, our station distribution is dense enough to avoid this problem, except on the edges of the array. As the coda is composed mainly of surface waves at the periods we are considering, leakage of coda into the mantle as described in Margerin *et al*. (1999) should not be a significant factor. Indeed, the depth penetration of the surface waves is much smaller than Moho depth.

3 MAPPING OF CODA-Q

The main difficulty for transforming coda-Q measurements into a geographic distribution is that the area sampled by the coda is dependent on scattering regime. The additional propagation distance with respect to the great circle distance corresponds at the beginning of the coda wave window (120 s after the main arrival) to ∼360 km and at the end of the coda window (520 s after the main arrival) to ∼1560 km. It can therefore be expected that the beginning and the end of the coda are not in the same scattering regime.

Additionally, we know that the typical estimation of the mean free time in the crust is of the order of tens of seconds at 1 s period. Although the scattering coefficient decreases at longer periods, we do not expect single scattering (e.g. Xie & Mitchell 1990) to be the dominant mechanism at long lapse time in our data. Furthermore, we know from the work of Mayor *et al.* (2014) that the slope of intensity decay (hence coda-Q) is more sensitive to absorption than scattering, if scattering is isotropic. Usually scattering anisotropy manifests itself in the data at much shorter periods, hence the assumption of at least partial dominance of absorption over scattering appears a fortiori valid for the ambient noise coda. The pattern of spatial sensitivity to absorption shown by Mayor *et al.* (2014) is dominated by singularities located at the source and receiver and local maxima located on the direct ray connecting the source to the station. Although our measurements are very likely influenced by the scattering properties, it is not unreasonable to expect a single coda-Q (Q_c) measurement to be more sensitive to the attenuation structure in a (broad) region encompassing the source and the receiver. In any event, we know that the sensitivity is not uniform in the single-scattering ellipse but rather concentrated around specific locations.

However, before mapping, we made sure that there are discernible geographic patterns of the individual coda-Q measurements. This is illustrated by Fig. 7 which shows the geographic distribution of observed coda-Q. We plot the rays joining each couple of stations, colouring them according to the corresponding coda-Q value. For Fig. 7, as for all the following, we use only correlations over distances between 50 and 200 km. In the 2.5–5 s and 5–10 s period bands, in spite of some scatter, we clearly identify regions of high and low coda-Q values. On the contrary, the scatter in the 10–20 s period band is too high to reveal geographic tendencies with this type of plot.

An alternative visualization, shown in Fig. 8, is to plot the mean coda-Q per station: to each station we attribute the geometric mean of coda-Q ($10^{\frac{\sum^{\log}(coda-Q)}{N}}$, i.e. averaging over the logarithm of coda-Q) of all correlations that involve this station. We choose this mean because of its lower sensitivity to outliers and because of the exponential nature of coda-Q. We plot results only for stations with more than 5 coda-Q measurements. As expected, the pattern is very similar to that of Fig. 7, but geographic patterns are more easily identified. A first result is that the contrasts in coda-Q decrease with period. This is expected if the coda is dominated by surface waves, as both lateral variations in intrinsic Q and variations in seismic velocities, leading to scattering, are relatively high within the uppermost part of the crust. We also observe that at long period (10–20 s) there is less geographic coherency between neighbouring stations, coherent with Fig. 7. This means that poor measurement quality (resulting in large uncertainty of coda-Q values) results in geographic dispersion of results which will not map into coherent geographic patterns.

On the contrary, in the 2.5–5 s and 5–10 s period bands, we observe clear geographic patterns, which are relatively similar. In both period bands, we observe the lowest coda-Q in northern Italy (Po Plain). We also observe areas of high coda-Q in the eastern Alps and in the south-westernmost part of the study area. There are also some differences between the two period bands. The most striking part is that the northwestern part of the study area is dominated by low coda-Q between 5 and 10 s, but less so between 2.5 and 5 s.

To perform mapping, we choose the approach by Mayor *et al.* (2016), who map coda-Q onto the rays between the stations. In this method, the study area is divided into cells and to each cell we attribute the mean value (geometric mean) of the coda-Q of the rays crossing the cell. In each cell, values higher or lower than three times the standard deviation (calculated independently for each cell) are excluded.

We implemented an adaptive grid based on Schaefer *et al.* (2011). Rather than merging cells, we start with a single cell. At each iteration, we subdivide any cell into four if it (i) is crossed by at least ten rays and (ii) has at least three rays in at least three of the azimuth intervals 0°–45°, 45°–90°, 90°–135° and 135°–180°. If three of the four resulting subcells satisfy the same criteria, we keep this finer grid. The process is iterated for each cell until no subdivision is possible using the above criteria, or if the subcells become smaller than one wavelength. With this approach we ensure a good azimuthal coverage within each cell, to avoid any potential bias. This is a conservative procedure, as we already check for the absence of coda-Q dependency on azimuth (see Fig. 6).

The results of the mapping are shown in Fig. 9. As standard deviations in each cell are calculated using the logarithm of

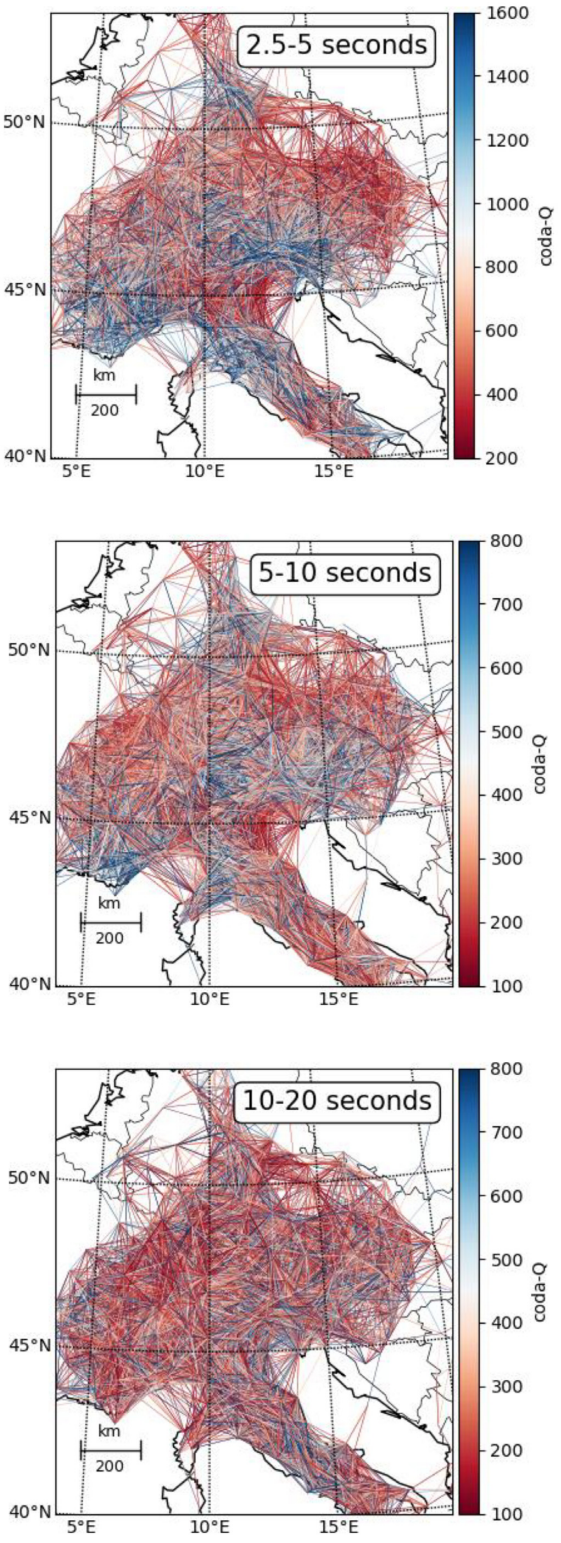

Figure 7. Maps of coda-Q measured for each station pair. Each path between pairs of stations is coloured according to the observed coda-Q (note the difference of colour scale in different period intervals). Only correlations with interstation distances comprised between 50 and 200 km are used. Note that between 25 and 40 per cent of all correlation pass all selection criteria for both the causal and anticausal parts and will therefore not show on these kind of plots, as one covers the other. A geographic pattern clearly emerges in the two period bands 2.5–5 s and 5–10 s, whereas geographic patterns remain speculative in the 10–20 s period band.

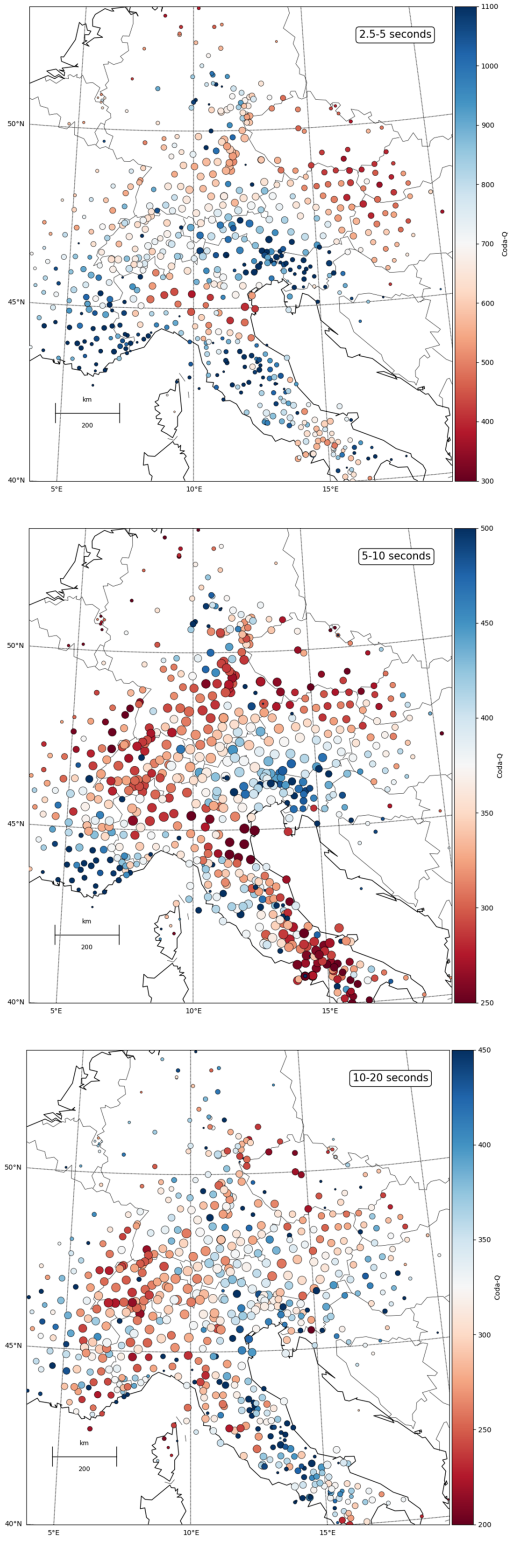

Figure 8. Average coda-Q (colour scale) per station (circles). For each station that has more than five measurements of coda-Q, the average has been calculated by calculating the mean of log10(coda-Q) excluding all measurements further than 2 standard deviations away from the average and calculating the power of 10 of the resulting mean. The size of the circle indicates the number of correlations used in the average. Only pairs with interstation distances between 50 and 200 km are used. As in Fig. 7, we see a clear pattern in the two first period bands, while the results in the 10–20 s period band are more randomly distributed.

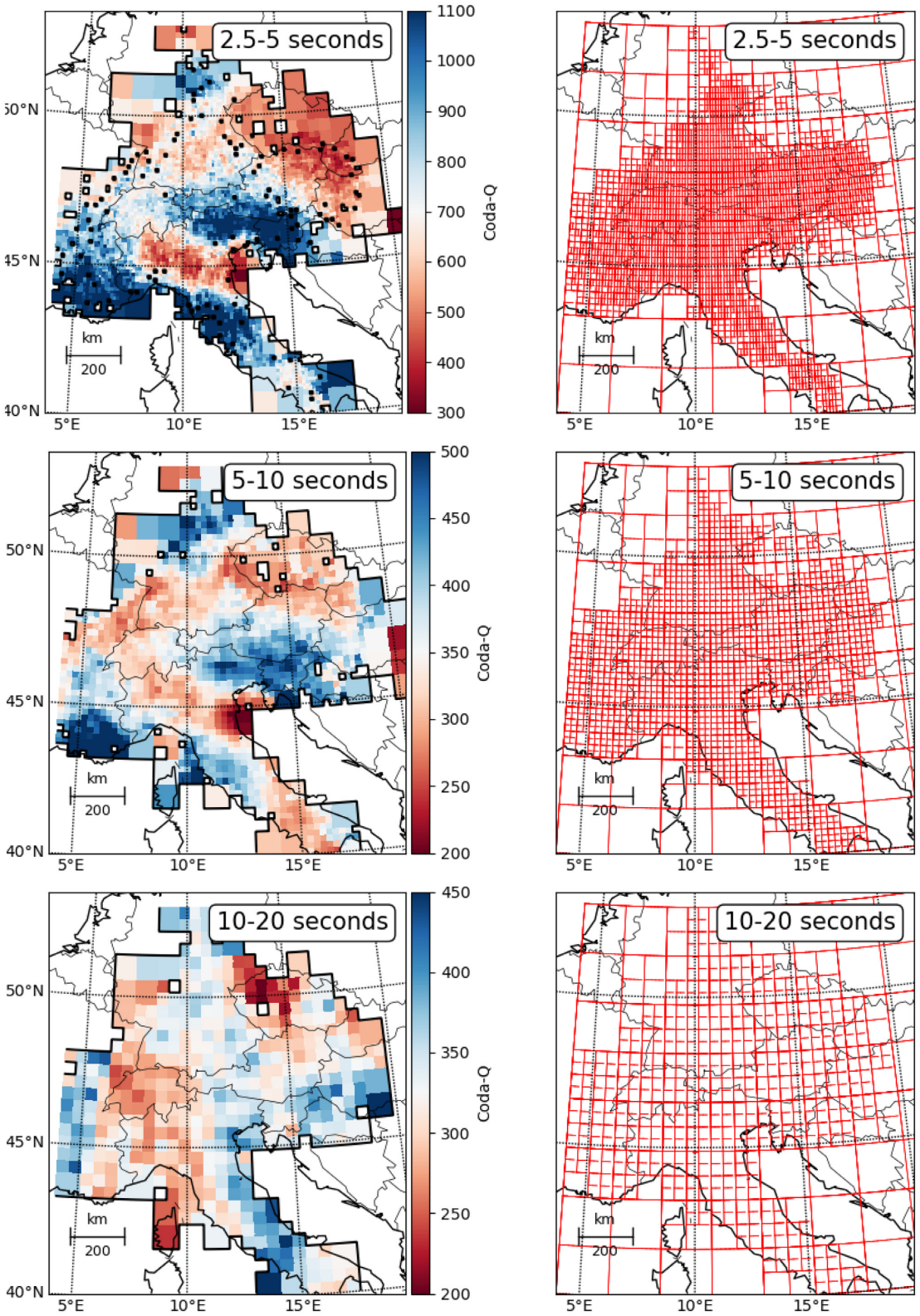

Figure 9. Left-hand panel: maps of coda-Q. Right-hand panel: adaptive grid. Note that the colour scale is not the same in all period bands. Rays are not drawn in the adaptive grid because of the very high ray density in most of the region.

coda-Q, we cannot map the standard deviations in a meaningful way. The map of log10(coda-Q) and associated standard deviations are shown in Fig. S2. Note that the standard deviations show that in the frequency bands 2.5–5 s and 5–10 s, the geographic pattern of high and low coda-Q is resolved but interpretation of small-scale variations of coda-Q needs to be associated with stability tests. For 10–20 s the standard deviations are such that the apparent geographic patterns in Fig. 9 are barely resolved, but our results hint

that it may be possible to obtain coda-Q information also in this period interval.

Fig. 9 confirms the previous observation that the amplitude of the variations is larger at short period than at long periods. This observation is coherent with the strong heterogeneities in the uppermost crust, notably the deep sedimentary basins.

To understand the geographic pattern of the coda-Q observations, Fig. 10 shows the map of coda-Q between 2.5 and 5 s period overlaying the topographic map and the map of sedimentary basins (see Fig. 1). The maps shows an excellent definition of the Po Plain as a low coda-Q area (∼400–600) while the Alps and the Apennines are characterized by high coda-Q (>800). This is in overall agreement with Mayor *et al*. (2016), but with our data providing a better resolution. Note that the area of Lg blockage in the Western Alps (Campillo *et al*. 1993) is known to be very small so can not be resolved. There is a small part of the Swiss Alps, NW of the Po Plain, where coda-Q is of the order of 700. In the Swiss Alps it is likely that the combination of narrow lateral extension, nearby low coda-Q and orientation in the direction of the dominant noise source direction is the cause of the artificially low coda-Q. We tentatively estimated the severity of potential smearing from the Po Plain in a 1° longitude x 0.5° latitude grid, where in each gridpoint we estimated the variations of coda-Q with azimuth. This analysis showed that smearing may be a problem in this area, and along the northern edge of the Po Plain. Similar problems occur in isolated spots along the edge of the array.

Other observations are moderately low coda-Q in the wider part of the Molasse Basin, while the narrowest part (SW part) does not have particularly low coda-Q. We infer from this pattern that this part of the basin is too narrow to be resolved. The same is the case for the Rhine Graben and the Rhone Valley. The Pannonian Basin, on the edge of the resolved area, is characterized by low coda-Q in the 2.5–5 s period band, less so in the 5–10 s period band. Two observations are surprising: the first one is that the Bohemian Massif shows low coda-Q, in contradiction to Gäbler *et al.* (2015). However, as can be seen in Fig. 1, the station density in this area is lower than the rest of the study area, and as a consequence the ray coverage is relatively poor, as can be seen on the ray density (Fig. 7) and plotting grid (Fig. 9). Secondly, we observe, in contrast with the results of Mayor *et al*. (2016), that the South East French Basin, shown as a sedimentary basin in the south westernmost part of the resolved area, has high coda-Q. The equivalent map for 5–10 s period (Fig. S3) overall has the same features as Fig. 10.

4 IMPACT OF DATA QUALITY AND TIME SERIES LENGTH

4.1 Effect of further data selection

One specific concern about coda-Q obtained from noise correlations is the influence of data quality on the coda-Q values and maps. To evaluate the impact of data selection on observed coda-Q, we compare our results to those of a further reduced data set obtained by applying additional selection criteria. The thresholds for data rejection are adapted in each period band to ensure sufficient data for the mapping. The following selection criteria and associated thresholds are applied:

1. Reject all traces with SNR below 500 (300 for period band 2.5–5 s).

2. Reject all unstable coda-Q measurements. To estimate the stability of observed coda-Q, we perform a second measurement with a different coda window length (300 s instead of 400 s for period bands 2.5–5 s and 5–10 s; 400 s instead of 600 s for period band 10–20 s) and compare it to the initial measurement. If $Q_{400\,s}/Q_{300\,s}$ ($Q_{600\,s}/Q_{400\,s}$ for the period band 10–20 s) is outside a defined range $[1/R;R]$, the measurement is rejected. R had to be adapted as the threshold for rejecting almost all measurements is different in the three period bands. We choose it as $R = 3$ (2.5–5 s), $R = 2$ (5–10 s) and $R = 1.25$ (10–20 s).

3. Reject all correlations that are stacked over less than 200 d. This criteria is related to the convergence rate of coda-Q, specifically discussed in Section 4.2.

After application of these criteria, the remaining number of traces is 6572 (2.5–5 s), 8466 (5–10 s) and 3314 (10–20 s) which represent approximately 0.5 per cent of the initial data set. On this reduced data set coda-Q is independent of azimuth and distance in the 50–200 km distance range, as opposed to the bias towards higher coda-Q on longer distances on the initial data set. The map based on this reduced data set is shown in Fig. 11. This map has a significantly poorer lateral resolution (increased cell size) than the one of Fig. 9, but overall the geographic pattern remains identical and the standard deviation on log(coda-Q) is significantly smaller. The stricter data selection does however show one systematic difference: coda-Q has overall decreased, mostly in areas with high coda-Q. Therefore, care should be taken on the absolute values of coda-Q measured on noise correlations.

4.2 Convergence of Coda-Q

It is generally agreed that correlating 1 yr (or sometimes much less) of ambient-noise data is sufficient to obtain a stable main arrival (e.g. Sabra *et al.* 2005) but the convergence of coda-Q observed on noise correlations is not well known. Fig. 12 shows the density distribution of $Q(t)/Q_4$ and $Q(t)/Q_1$ for selected station pairs. Q_4 and Q_1 are coda-Q measured for 4 yr of data (January 2014–October 2018, Fig. 12a) and for 1 yr of data (July 2016 to June 2017, Fig. 12b). The selected station pairs are those of permanent stations, for which the correlations are accepted in the hyper-reduced data set used in Fig. 11. $Q(t)$ is coda-Q made on stacks of t days of data. Note that when a station pair does not have 4 (or 1) yr of data, Q_4 and Q_1 use the maximum number of days available, and the station pair is not counted beyond the last day.

Fig. 12 shows two main phenomena. The first one is that convergence is slow, and that at least 200 d are necessary for convergence. We verified that convergence is independent of both azimuth and distance. The second observation is that convergence is systematically from higher coda-Q towards lower coda-Q. This means that coda-Q will decrease over time until convergence is reached and bias will be systematically towards higher coda-Q. This is expected as noise (in the sense of true noise) has stable amplitude with time, hence a poor coda/noise level should lead to higher coda-Q. The faster convergence of coda-Q for lower coda-Q values is a natural consequence of the measurement stability of a steep slope.

Fig. 13(a) shows the distribution of Q_1/Q_4. By plotting Q_1/Q_4 separately for $100 < Q_1 < 150$ and $400 < Q_1 < 1000$, we confirm that the bias is stronger for high coda-Q values. It is possible to map this bias by plotting Q_1 as a function of Q_4, using the median value of Q_1 and Q_4 for data in different intervals of Q_1 (Fig. 13c, see caption for details). We confirm that high coda-Q values are likely to be overestimated when we use the AlpArray data set, for which we use 1 yr of data. On the other hand, geographic distribution of high and low coda-Q regions is not affected.

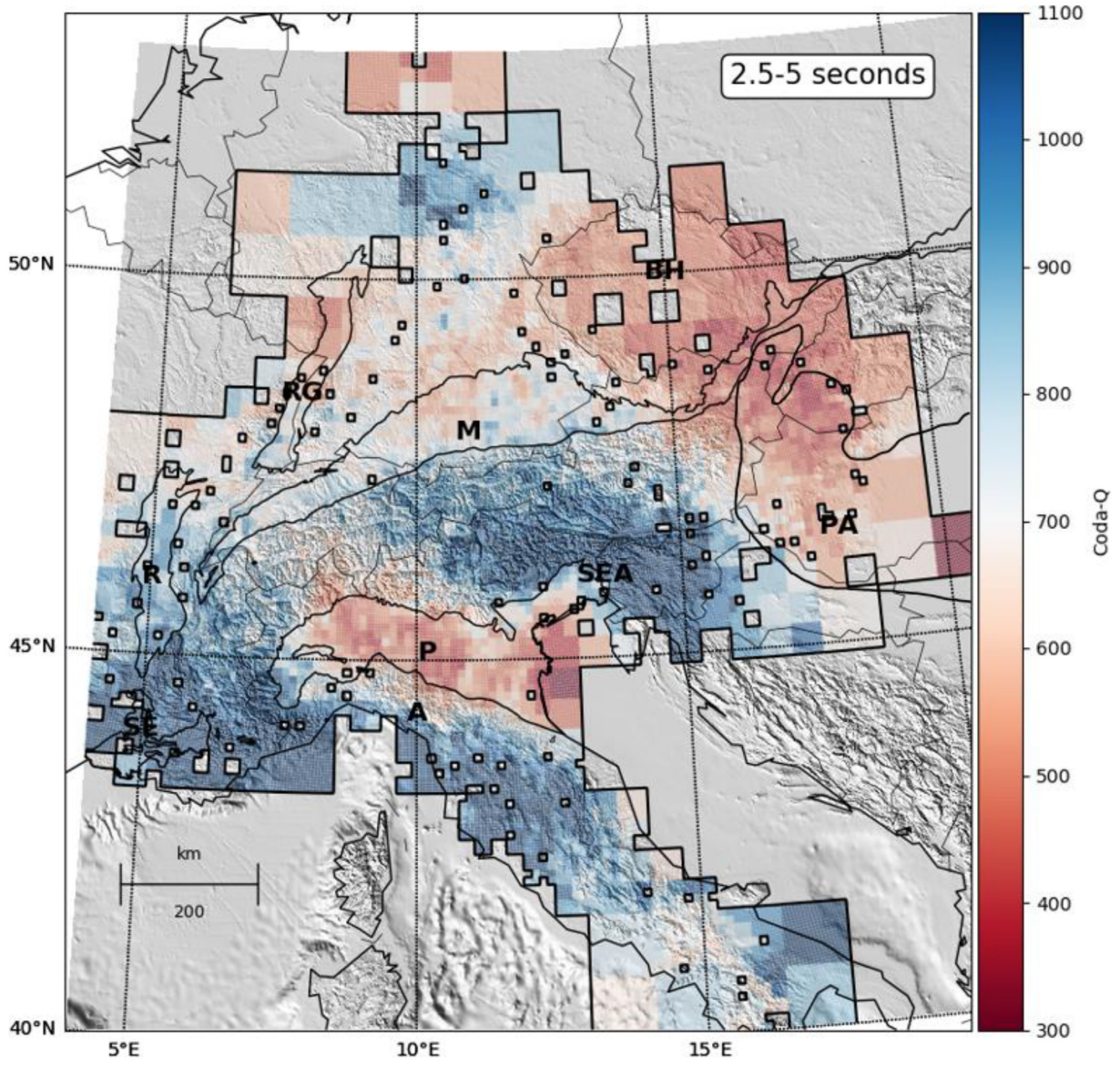

Figure 10. Map of coda-Q overlain onto the topography and main sedimentary basins (see Fig. 1, and caption to Fig. 1).

5 DISCUSSION AND CONCLUSIONS

In the present article, we use the correlations of ambient noise to extract coda-Q in the period range 2.5–20 s. No such measures have been made in this period band previously because of the high amplitude of the seismic noise that makes measures on earthquake coda very difficult. This difficulty transforms into a strength in the case of noise correlations, due to a particularly high signal to noise ratio of the correlations in this period band. We are able to obtain a stable geographic pattern of high and low coda-Q across the greater Alpine region, independently of whether we apply data selection criteria where 15 or 1 per cent of the data are used for the mapping. This result is confirmed in the 2.5–5 s and 5–10 s period bands while our results in the 10–20 s period band remain speculative.

Another strength of the noise correlations is that a dense seismic network will yield a high resolution image of coda-Q. In our case, the high resolution is achieved by combining data from permanent seismic broad-band stations in the greater Alpine area with temporary AlpArray stations. One of the potential difficulties that we had to consider was whether the strong heterogeneity of the incoming noisefield, and in particular the high energy influx from the northwest (Atlantic Ocean noise sources) would bias the measurements. Our results demonstrate that at shorter distances (50–200 km), coda-Q is independent of azimuth while there were systematic variations of coda-Q with azimuth at longer distances. This type of test should be systematically applied to all coda-Q measurements using noise correlations. The influence of the Po Plain on coda-Q in the Swiss Alps, and the uncertainty on the low coda-Q in the Bohemian Massif also shows that we need to develop further tools to better understand the conditions under which coda-Q is well constrained.

While the geographic pattern is very stable, the numerical values of coda-Q strongly depend on data selection and the duration of the time-series used for the correlations. In particular, severe data selection (e.g. in terms of SNR) results in a decrease of coda-Q. Further studies on longer time-series show that low coda-Q values

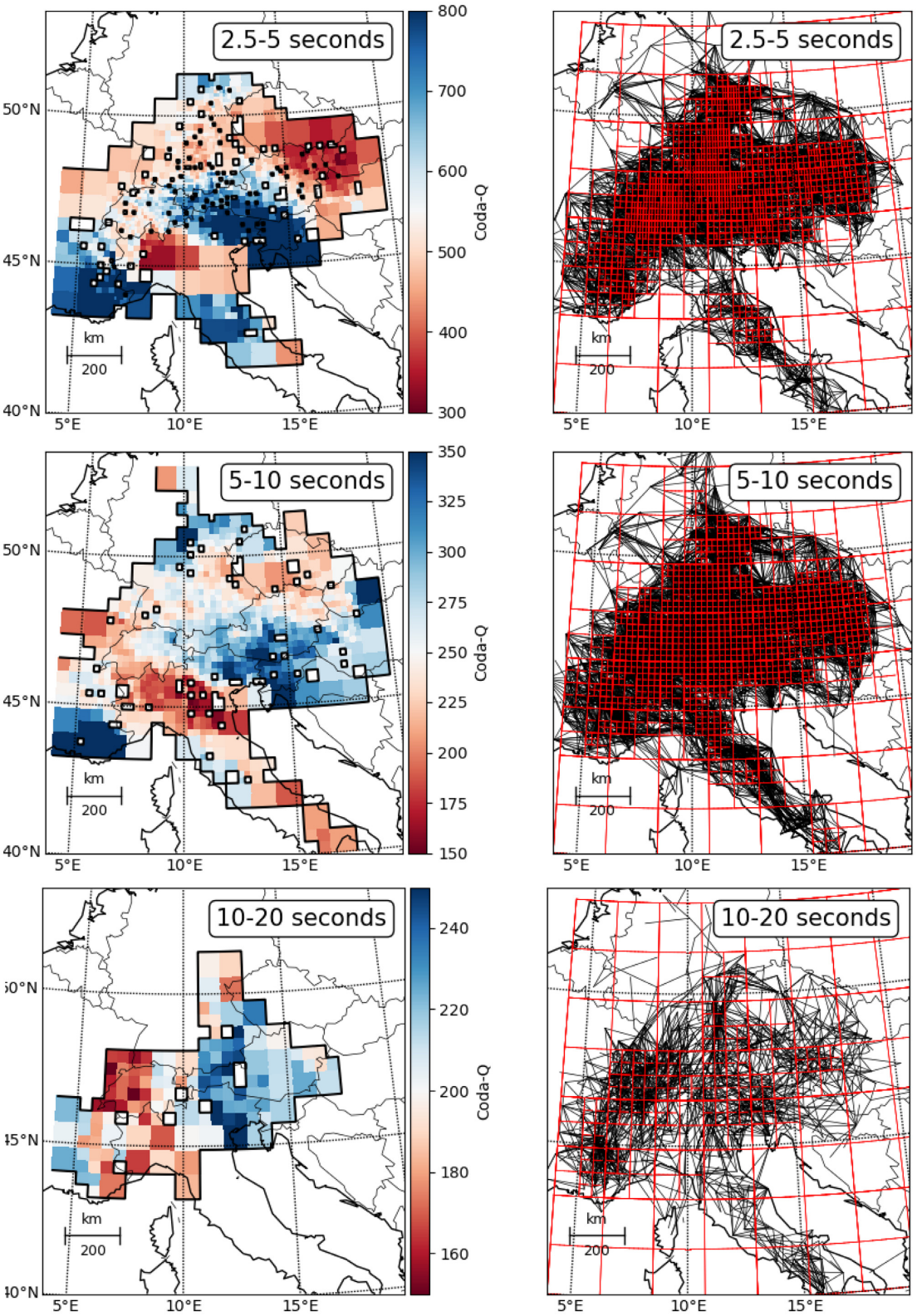

Figure 11. Left-hand panel: maps of coda-Q using the further reduced data set (see Section 4.1 for selection criteria). Right-hand panel: path coverage and adaptive grid. Note that the colour scale is not the same in all period bands.

tend to stabilize faster than high coda-Q values, but a minimum of 200 d of continuous recording is still required. Consequently, the numerical values of coda-Q in the high coda-Q areas may be overestimated. Another consequence is that longer time series must be used to test the possibility of stable measurements in the 10–20 s period range, where there is an observed coda in the correlations. At periods longer than 20 s, we did not observe any coda, but time series spanning over several years might achieve a sufficient signal

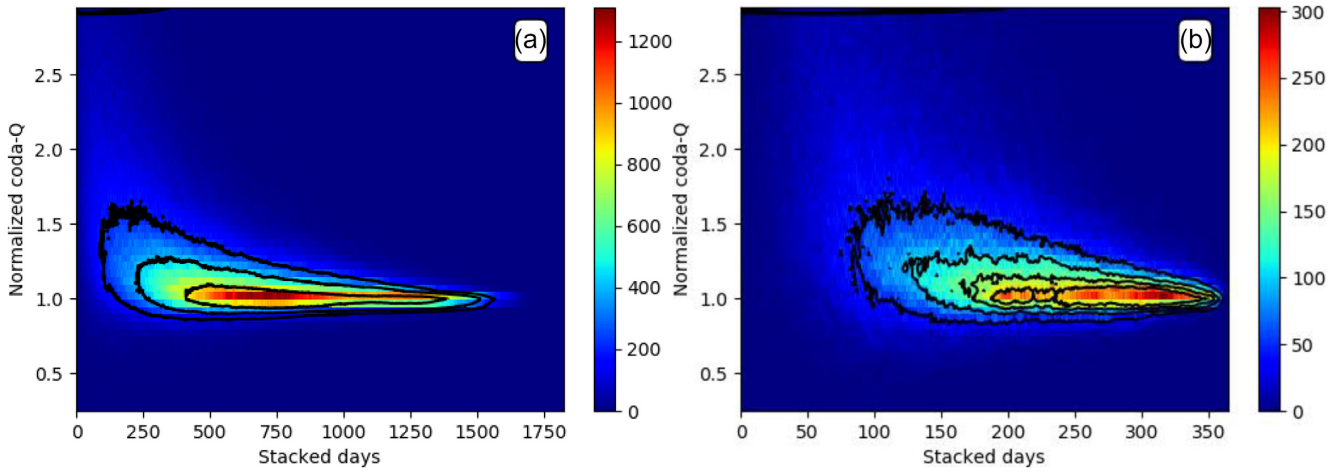

Figure 12. Coda-Q convergence as a function of the number of days stacked using (a) the 4-yr data set and (b) the 1-yr data set (station pairs for which less than 200 d are available are not shown) in the 5–10 s period band. For each station pair we calculate coda-Q using an increasing number of days in the stack, and normalized with the coda-Q obtained using all days available for the station pair. Note that the 4-yr data set has on average 3 yr of daily correlations with coda-Q measurements for any given station pair. This Fig. shows a systematic bias towards high coda-Q when averaging is insufficient.

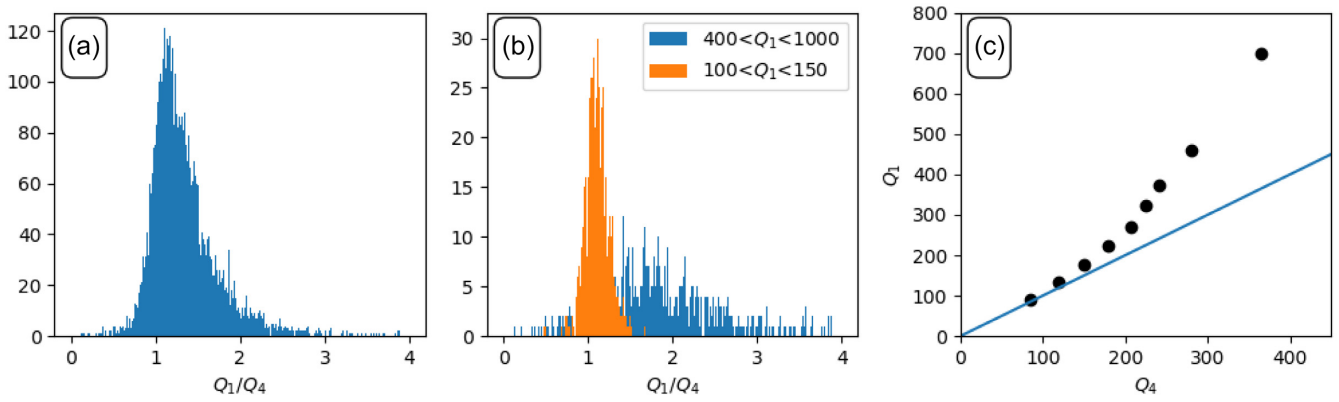

Figure 13. Coda-Q bias with time series length. (a) Histograms of the ratio of coda-Q calculated with the 1-yr (Q_1) and the 4-yr (Q_4) data set for identical station pairs. (b) Same plot but using only data with low Q_1 (orange) or high Q_1 (blue). (c) Based on separation into Q_1 intervals (1 yr results, bins 0–100, 100–150, 150–200, 200–250, 300–350, 350–400, 400–600 and 600–1000), plot of the median of Q_1 as a function of the median of Q_4 using the same station pairs. The blue line corresponds to equal Q_1 and Q_4. With the simple increase as a function of Q_4 we consider that high values of coda-Q may be overestimated, but that our results reflect contrasts between high coda-Q and low coda-Q.

to noise ratio to observe a stable coda at longer periods (20–40 s). At very long periods, it is known from earthquake studies that the Rayleigh wave coda is small.

Whilst caution should be taken as to the numerical values of coda-Q, we do observe that coda-Q decreases with period (∼750 at 2.5–5 s period, ∼350 at 5–10 s period, ∼330 at 10–20 s period). This decrease is coherent with observations from other studies (Aki & Chouet 1975; Mayor *et al*. 2016), but our observations do not extrapolate to meet those of Mayor *et al*. (2016) who observe earthquake data coda-Q of ∼200 at 1–2 Hz in the area. While the geographic distribution of high and low coda-Q is in overall agreement with Mayor et al. (2016), there are also differences for example in the SE France basin. A possible explanation is the difference in the characteristics of the noise field (containing predominantly surface waves) compared to the short-period earthquake wavefield (containing predominantly body waves) so that the two studies may be sampling different depths in the medium. Additionally, the propagation regime of ambient noise coda is probably different from the one of earthquake coda as we expect scattering at longer period to be weaker than at high frequency.

More work remains to better characterize the physical meaning of the observations. Regardless of the avenues to further explore, this work demonstrates that noise cross-correlations can provide a new type of observation for seismic imaging.

6 ORIGIN OF DATA

Waveform data used in this paper belong to the permanent networks with codes AC, BE (Royal Observatory of Belgium 1985), BW (Department of Earth and Environmental Sciences, Geophysical Observatory, University of München 2001), CA (Institut Cartogràfic i Geològic de Catalunya-Institut d'Estudis Catalans 1996), CH [Swiss Seismological Service (SED) at ETH Zürich 1983], CR, CZ (Institute of Geophysics, Academy of Sciences of the Czech Republic 1973), ES (Instituto Geografico Nacional, Spain 1999), FR (RESIF 1995), G [Institut de Physique du Globe de Paris (IPGP) and Ecole et Observatoire des Sciences de la Terre de Strasbourg (EOST) 1982], GE (GEOFON Data Centre 1993), GR [Federal Institute For Geosciences And Natural Resources (BGR) 1976], GU

(University of Genova 1967), HU (Kövesligethy Radó Seismological Observatory 1992), II (Scripps Institution of Oceanography 1986), IV (INGV Seismological Data Centre 2006), IX, MN (MedNet Project Partner Institutions 1990), NI [OGS (Istituto Nazionale di Oceanografia e di Geofisica Sperimentale) and University of Trieste 2002], NL (KNMI 1993), OE (ZAMG—Zentralanstalt für Meterologie und Geodynamik 1987), OT (University of Bari 'Aldo Moro' 2013), OX [OGS (Istituto Nazionale di Oceanografia e di Geofisica Sperimentale) 2016], RD (RESIF 2018), RF (University of Trieste 1993), SI, SJ, SK [ESI SAS (Earth Science Institute Of The Slovak Academy Of Sciences) 2004], SL (Slovenian Environment Agency 2001), ST (Geological Survey-Provincia Autonoma di Trento 1981), SX (Leipzig University 2001), TH (Friedrich Schiller University Jena and Thuringian Institute of Environment and Geology 2009), TT, WM [San Fernando Royal Naval Observatory (ROA), Universidad Complutense de Madrid (UCM), Helmholtz-Zentrum Potsdam Deutsches GeoForschungsZentrum (GFZ), Universidade de Evora (UEVORA, Portugal), & Institute Scientifique of RABAT (ISRABAT, Morocco) 1995]. We also used data of the temporary AlpArray network (network code Z3 2015; AlpArray Seismic Network 2015).

ACKNOWLEDGEMENTS

We gratefully thank the operators of the European permanent seismic networks who make their data available through EIDA (http://www.orfeus-eu.org/eida). The Z3 network is operated by the AlpArray Seismic Network Team: György Hetényi, Rafael Abreu, Ivo Allegretti, Maria-Theresia Apoloner, Coralie Aubert, Maxime Bes De Berc, Götz Bokelmann, Didier Brunel, Marco Capello, Martina Čarman, Adriano Cavaliere, Jérôme Chèze, Claudio Chiarabba, John Clinton, Glenn Cougoulat, Wayne Crawford, Luigia Cristiano, Tibor Czifra, Ezio D'Alema, Stefania Danesi, Romuald Daniel, Iva Dasović, Anne Deschamps, Jean-Xavier Dessa, Cécile Doubre, Sven Egdorf, ETHZ-SED Electronics Lab, Tomislav Fiket, Kasper Fischer, Wolfgang Friederich, Florian Fuchs, Sigward Funke, Domenico Giardini, Aladino Govoni, Zoltán Grácz er, Gidera Gröschl, Stefan Heimers, Ben Heit, Davorka Herak, Marijan Herak, Johann Huber, Dejan Jarić, Petr Jedlička, Yan Jia, Hélène Jund, Edi Kissling, Stefan Klingen, Bernhard Klotz, Petr Kolínský, Michael Korn, Josef Kotek, Lothar Kühne, Krešo Kuk, Jürgen Loos, Deny Malengros, Lucia Margheriti, Christophe Maron, Xavier Martin, Marco Massa, Francesco Mazzarini, Thomas Meier, Laurent Métral, Irene Molinari, Milena Moretti, Helena Munzarová, Anna Nardi, Jurij Pahor, Anne Paul, Catherine Péquegnat, Damiano Pesaresi, Davide Piccinini, Claudia Piromallo, Thomas Plenefisch, Jaroslava Plomerová, Silvia Pondrelli, Snježan Prevolnik, Roman Racine, Marc Régnier, Miriam Reiss, Joachim Ritter, Georg Rümpker, Simone Salimbeni, Detlef Schulte-Kortnack, Werner Scherer, Sven Schippkus, Vesna Šipka, Daniele Spallarossa, Kathrin Spieker, Josip Stipčević, Angelo Strollo, Bálint Süle, Gyöngyvér Szanyi, Eszter Szücs, Christine Thomas, Frederik Tilmann, Stefan Ueding, Massimiliano Vallocchia, Luděk Vecsey, René Voigt, Joachim Wassermann, Zoltán Wéber, Christian Weidle, Viktor Wesztergom, Gauthier Weyland, Stefan Wiemer, David Wolyniec, Thomas Zieke and Mladen Živčić. All data processing is carried out with python software, and the community software Obspy (Krischer *et al.* 2015) is used for many of the operations. We also thank Pierre Boué for his valuable help in the calculation of the correlations and his insight in the physical meaning of cross-correlations. We also thank Ulrich Wegler and an anonymous reviewer for their helpful comments. This manuscript was greatly improved thanks to their constructive feedback. This work is part of the project AlpArray-FR funded by Agence Nationale de la Recherche (contract ANR-15-CE31-0015), Labex OSUG@2020 (Investissement d'Avenir, ANR-10-LABX-56) and by the European Research Council under the European Union Horizon 2020 research and innovation program (grant agreement 742335–F-IMAGE).

REFERENCES

Aki, K. & Chouet, B., 1975. Origin of coda waves: source, attenuation, and scattering effects, *J. geophys. Res.,* **80,** 3322–3342.

AlpArray Seismic Network, 2015. AlpArray Seismic Network (AASN) temporary component. AlpArray Working Group. doi:10.12686/ALPARRAY/Z3_2015

Anache-Menier, D., Tiggelen, B.A. van & Margerin, L., 2009. Phase statistics of seismic coda waves, *Phys. Rev. Lett.,* **102,** 248501.

Calvet, M. & Margerin, L., 2013. Lapse-time dependence of coda Q: anisotropic multiple-scattering models and application to the Pyrenees, *Bull. seism. Soc. Am.,* **103,** 1993–2010.

Campillo, M., Feignier, B., Bouchon, M. & Béthoux, N., 1993. Attenuation of crustal waves across the Alpine Range, *J. geophys. Res.: Solid Earth,* **98,** 1987–1996.

Campillo, M. & Paul, A., 2003. Long-range correlations in the diffuse seismic coda, *Science,* **299,** 547–549.

Carcole, E. & Sato, H., 2010. Spatial distribution of scattering loss and intrinsic absorption of short-period S waves in the lithosphere of Japan on the basis of the Multiple Lapse Time Window Analysis of Hi-net data, *Geophys. J. Int.,* **180,** 268–290.

Colombi, A., Chaput, J., Brenguier, F., Hillers, G., Roux, P. & Campillo, M., 2014. On the temporal stability of the coda of ambient noise correlations, *C.R. Geosci.,* **346,** 307–316.

Cupillard, P. & Capdeville, Y., 2010. On the amplitude of surface waves obtained by noise correlation and the capability to recover the attenuation: a numerical approach, *Geophys. J. Int.,* **181,** 1687–1700.

Denolle, M.A., Dunham, E.M., Prieto, G.A. & Beroza, G.C., 2013. Ground motion prediction of realistic earthquake sources using the ambient seismic field, *J. Geophys. Res.: Solid Earth,* **118,** 2102–2118.

Department of Earth and Environmental Sciences, Geophysical Observatory, University of Munchen, 2001. BayernNetz. International Federation of Digital Seismograph Networks. Data set/Seismic Network. doi:10.7914/SN/BW

ESI SAS (Earth Science Institute of the Slovak Academy of Sciences), 2004. National Network of Seismic Stations of Slovakia. Deutsches GeoForschungsZentrum GFZ. Other/Seismic Network. doi:10.14470/FX099882.

Federal Institute For Geosciences And Natural Resources (BGR), 1976. *German Regional Seismic Network (GRSN)*. Federal Institute for Geosciences and Natural Resources (BGR). doi:10.25928/mbx6-hr74

Fehler, M., Hoshiba, M., Sato, H. & Obara, K., 1992. Separation of scattering and intrinsic attenuation for the Kanto-Tokai region, Japan, using measurements of *S* -wave energy versus hypocentral distance, *Geophys. J. Int.,* **108,** 787–800.

Friedrich, A., Krüger, F. & Klinge, K., 1998. Ocean-generated microseismic noise located with the Gräfenberg array, *J. Seismol.,* **2,** 47–64.

Friedrich Schiller University Jena and Thuringian Institute of Environment and Geology, 2009. Thüringer Seismologisches Netz (TSN). International Federation of Digital Seismograph Networks. Dataset/Seismic Network. doi:10.7914/SN/TH

Gäbler, P.J., Eulenfeld, T. & Wegler, U., 2015. Seismic scattering and absorbtion parameters in the W-Bohemia/Vogtland region from elastic and acoustic radiative transfer theory, *Geophys. J. Int.,* **203,** 1471–1481.

GEOFON Data Centre, 1993. GEOFON Seismic Network. Deutsches GeoForschungsZentrum GFZ.Other/Seismic Network. doi:10.14470/TR560404.

Geological Survey-Provincia Autonoma di Trento. 1981. Trentino Seismic Network. International Federation of Digital Seismograph Networks. Dataset/Seismic Network. doi:10.7914/SN/ST.

GEOSCOPE - French Global Network of broadband seismic stations, 1982. Institut de Physique du Globe de Paris & Ecole et Observatoire des Sciences de la Terre de Strasbourg (EOST) - doi:10.18715/GEOSCOPE.G.

Herraiz, M. & Espinosa, A.F., 1987. Coda waves: a review, *Pure appl. Geophys. PAGEOPH,* **125,** 499–577.

Hetényi, G. *et al.*, 2018. The AlpArray Seismic Network: a large-scale european experiment to image the alpine orogen, *Surv. Geophys.,* **39,** 1009–1033.

Hillers, G., Graham, N., Campillo, M., Kedar, S., Landès, M. & Shapiro, N., 2012. Global oceanic microseism sources as seen by seismic arrays and predicted by wave action models: global oceanic microseism sources, *Geochem. Geophys. Geosyst.,* **13,** n/a–n/a. doi:10.1029/2011GC003875

INGV Seismological Data Centre, 2006. *Rete Sismica Nazionale (RSN)*. Istituto Nazionale di Geofisica e Vulcanologia (INGV), Italy. doi:10.13127/sd/x0fxnh7qfy

Institut Cartogràfic i Geològic de Catalunya-Institut d'Estudis Catalans, 1996. Catalan Seismic Network. International Federation of Digital Seismograph Networks. Dataset/Seismic Network. doi:10.7914/SN/CA

Instituto Geografico Nacional, Spain, 1999. Spanish Digital Seismic Network. International Federation of Digital Seismograph Networks. Dataset/Seismic Network. doi:10.7914/SN/ES.

Institute of Geophysics, Academy of Sciences of the Czech Republic, 1973. Czech Regional Seismic Network. International Federation of Digital Seismograph Networks. Other/Seismic Network. doi:10.7914/SN/CZ.

Kedar, S., Longuet-Higgins, M., Webb, F., Graham, N., Clayton, R. & Jones, C., 2008. The origin of deep ocean microseisms in the North Atlantic Ocean, *Proc. Royal Soc., A: Math,, Phys, Eng, Sci,,* **464,** 777–793.

KNMI, 1993. Netherlands Seismic and Acoustic Network. Royal Netherlands Meteorological Institute (KNMI). Other/Seismic Network. doi:10.21944/e970fd34-23b9-3411-b366-e4f72877d2c5.

Kövesligethy Radó Seismological Observatory (Geodetic and Geophysical Institute, Research Centre for Astronomy and Earth Sciences, Hungarian Academy of Sciences (MTA CSFK GGI KRSZO)), 1992. Hungarian National Seismological Network. Deutsches GeoForschungsZentrum GFZ. Other/Seismic Network. doi:10.14470/UH028726.

Krischer, L., Megies, T., Barsch, R., Beyreuther, M., Lecocq, T., Caudron, C. & Wassermann, J., 2015. ObsPy: a bridge for seismology into the scientific Python ecosystem, *Comput. Sci. Discov.,* **8,** 014003. doi:10.1088/1749-4699/8/1/014003.

Landès, M., Hubans, F., Shapiro, N.M., Paul, A. & Campillo, M., 2010. Origin of deep ocean microseisms by using teleseismic body waves, *J. geophys. Res.,* **115**. doi:10.1029/2009JB006918

Leipzig University, 2001. SXNET Saxon Seismic Network. International Federation of Digital Seismograph Networks. Dataset/Seismic Network. doi:10.7914/SN/SX.

Liu, X., Ben-Zion, Y. & Zigone, D., 2015. Extracting seismic attenuation coefficients from cross-correlations of ambient noise at linear triplets of stations, *Geophys. J. Int.,* **203,** 1149–1163.

Margerin, L., Campillo, M., Shapiro, N.M. & Tiggelen, B. van, 1999. Residence time of diffuse waves in the crust as a physical interpretation of coda Q : application to seismograms recorded in Mexico, *Geophys. J. Int.,* **138,** 343–352.

Mayor, J., Calvet, M., Margerin, L., Vanderhaeghe, O. & Traversa, P., 2016. Crustal structure of the Alps as seen by attenuation tomography, *Earth planet. Sci. Lett.,* **439,** 71–80.

Mayor, J., Margerin, L. & Calvet, M., 2014. Sensitivity of coda waves to spatial variations of absorption and scattering: radiative transfer theory and 2-D examples, *Geophys. J. Int.,* **197,** 1117–1137.

MedNet Project Partner Institutions, 1990. Mediterranean Very Broadband Seismographic Network (MedNet). Istituto Nazionale di Geofisica e Vulcanologia (INGV), Italy. doi:10.13127/sd/fbbbtdtd6q

Mikesell, T.D., Wijk, K. van, Blum, T.E., Snieder, R. & Sato, H., 2012. Analyzing the coda from correlating scattered surface waves, *J. acoust. Soc. Am.,* **131,** EL275–EL281.

Obermann, A., Larose, E., Margerin, L. & Rossetto, V., 2014. Measuring the scattering mean free path of Rayleigh waves on a volcano from spatial phase decoherence, *Geophys. J. Int.,* **197,** 435–442.

OGS (Istituto Nazionale di Oceanografia e di Geofisica Sperimentale), 2016. North-East Italy Seismic Network. International Federation of Digital Seismograph Networks. Dataset/Seismic Network. doi:10.7914/SN/OX

OGS (Istituto Nazionale di Oceanografia e di Geofisica Sperimentale) and University of Trieste, 2002. North-East Italy Broadband Network. International Federation of Digital Seismograph Networks. Dataset/Seismic Network. doi:10.7914/SN/NI.

Pedersen, H.A. & Krüger, F. the SVEKALAPKO Seismic Tomography Working Group, 2007. Influence of the seismic noise characteristics on noise correlations in the Baltic shield, *Geophys. J. Int.,* **168,** 197–210.

Poli, P., Pedersen, H.A. & Campillo, M. the POLENET/LAPNET Working Group, 2012. Emergence of body waves from cross-correlation of short period seismic noise: body waves from noise correlation, *Geophys. J. Int.,* **188,** 549–558.

Prieto, G.A. & Beroza, G.C., 2008. Earthquake ground motion prediction using the ambient seismic field, *Geophys. Res. Lett.,* **35,** L14304. doi:10.1029/2008GL034428

RESIF, 2018. CEA/DASE broad-band permanent network in metropolitan France, RESIF - Réseau Sismologique et géodésique Français. doi:10.15778/RESIF.RD.

RESIF, 1995, . RESIF-RLBP French Broad-band network, RESIF-RAP strong motion network and other seismic stations in metropolitan France. RESIF - Réseau Sismologique et géodésique Français. Seismic Network. doi:10.15778/RESIF.FR

Retailleau, L., Boué, P., Stehly, L. & Campillo, M., 2017. Locating microseism sources using spurious arrivals in intercontinental noise correlations, *J. geophys. Res.: Solid Earth,* **122,** 8107–8120.

Royal Observatory of Belgium, 1985. Belgian Seismic Network. International Federation of Digital Seismograph Networks. Other/Seismic Network. doi:10.7914/SN/BE

Sabra, K.G., Gerstoft, P., Roux, P., Kuperman, W.A. & Fehler, M.C., 2005. Surface wave tomography from microseisms in Southern California: SURFACE WAVE TOMOGRAPHY, *Geophys. Res. Lett.,* **32**.

San Fernando Royal Naval Observatory (ROA); Universidad Complutense De Madrid (UCM); Helmholtz-Zentrum Potsdam Deutsches GeoForschungsZentrum (GFZ); Universidade De Evora (UEVORA, Portugal); Institute Scientifique Of RABAT (ISRABAT, Morocco), 1995. The Western Mediterranean BB seismic Network. Deutsches GeoForschungsZentrum GFZ. Other/Seismic Network. doi:10.14470/JZ581150.

Schaefer, J.F., Boschi, L. & Kissling, E., 2011. Adaptively parametrized surface wave tomography: methodology and a new model of the European upper mantle: adaptively parametrized surface wave tomography, *Geophys. J. Int.,* **186,** 1431–1453.

Scripps Institution of Oceanography, 1986. IRIS/IDA Seismic Network. International Federation of Digital Seismograph Networks. Dataset/Seismic Network. doi:10.7914/SN/II.

Sens-Schönfelder, C. & Wegler, U., 2006. Passive image interferometry and seasonal variations of seismic velocities at Merapi Volcano, Indonesia, *Geophys. Res. Lett.,* **33**.

Shapiro, N.M. & Campillo, M., 2004. Emergence of broadband Rayleigh waves from correlations of the ambient seismic noise, *Geophys. Res. Lett.,* **31,** L07614.

Slovenian Environment Agency, 2001. Seismic Network of the Republic of Slovenia. International Federation of Digital Seismograph Networks. Dataset/Seismic Network. doi:10.7914/SN/SL.

Stanke, F.E. & Kino, G.S., 1984. A unified theory for elastic wave propagation in polycrystalline materials, *J. acoust. Soc. Am.,* **75,** 665–381.

Stehly, L., Campillo, M. & Shapiro, N.M., 2006. A study of the seismic noise from its long-range correlation properties, *J. geophys. Res.,* **111**.

Stehly, L. & Boue, P., 2017. On the interpretation of the amplitude decay of noise correlations computed along a line of receivers, *Geophys. J. Int.,* **209,** 358–372.

Swiss Seismological Service (SED) at ETH Zurich. 1983. National Seismic Networks of Switzerland; ETH Zürich. Other/Seismic Network. doi:10.12686/SED/NETWORKS/CH Datacite Link: http://data.datacite.org/10.12686/sed/networks/ch

University of Bari "Aldo Moro", 2013. OTRIONS, Seismic networks of Gargano Area (Italy). International Federation of Digital Seismograph Networks. Other/Seismic Network. doi:10.7914/SN/OT

University of Genova, 1967. Regional Seismic Network of North Western Italy. International Federation of Digital Seismograph Networks. Dataset/Seismic Network. doi:10.7914/SN/GU.

University of Trieste, 1993. Friuli Venezia Giulia Accelerometric Network. International Federation of Digital Seismograph Networks. Dataset/Seismic Network. doi:10.7914/SN/RF.

Wu, R. & Aki, K., 1988. Multiple-scattering and energy-transfer of seismic-waves - separation of scattering effect from intrinsic attenuation. 2. Application of the theory to Hindu Kush Region, *Pure appl. Geophys.,* **128,** 49–80.

Xie, J. & Mitchell, B.J., 1990. A back-projection method for imaging large-scale lateral variations of Lg coda Q with application to continental Africa, *Geophys. J. Int.,* **100,** 161–181.

ZAMG - Zentralanstalt für Meterologie und Geodynamik, 1987. Austrian Seismic Network. International Federation of Digital Seismograph Networks. Dataset/Seismic Network. doi:10.7914/SN/OE.

SUPPORTING INFORMATION

Supplementary data are available at *GJI* online.

Figure S1. Seismic section of correlations in the 2.5–5 s (left-hand panel), 5–10 s (centre panel) and 10–20 s (right-hand panel) period bands, for the selected data set (see Section 2.3). The traces are stacked in bins of 1 km and normalized by their maximum. All correlations have been oriented so that the causal part points away from 300° of azimuth; that is the direction which approximately corresponds to the dominant direction of the noise sources.

Figure S2. Map of log10 of coda-Q (left-hand panel) and its standard deviation in each cell (right-hand panel). As the distribution of log(coda-Q) is not Gaussian in the cells, the standard deviation only has indicative value.

Figure S3. Map of coda-Q superposed to topography and main sedimentary basins.

Please note: Oxford University Press is not responsible for the content or functionality of any supporting materials supplied by the authors. Any queries (other than missing material) should be directed to the corresponding author for the paper.